Galati *et al.*
EURASIP Journal on Advances in Signal Processing (2022) 2022:52
https://doi.org/10.1186/s13634-022-00884-1

EURASIP Journal on Advances in Signal Processing

REVIEW Open Access

Signal design and processing for noise radar

Gaspare Galati[1*], Gabriele Pavan[1] and Christoph Wasserzier[2]

*Correspondence:
gaspare.galati@uniroma2.it

[1] Tor Vergata University of Rome and CNIT-National Interuniversity Consortium for Telecommunications, via del Politecnico, 1, 00133 Rome, Italy
[2] Fraunhofer Institute for High Frequency Physics and Radar Techniques FHR, 53343 Wachtberg, Germany

Abstract

An efficient and secure use of the electromagnetic spectrum by different telecommunications and radar systems represents, today, a focal research point, as the coexistence of different radio-frequency sources at the same time and in the same frequency band requires the solution of a non-trivial interference problem. Normally, this is addressed with diversity in frequency, space, time, polarization, or code. In some radar applications, a secure use of the spectrum calls for the design of a set of transmitted waveforms highly resilient to interception and exploitation, i.e., with low probability of intercept/exploitation capability. In this frame, the noise radar technology (NRT) transmits noise-like waveforms and uses correlation processing of radar echoes for their optimal reception. After a review of the NRT as developed in the last decades, the aim of this paper is to show that NRT can represent a valid solution to the aforesaid problems.

Keywords: Radar signal processing, Waveform design, Noise radar technology, Ambiguity function, Low probability of intercept, Low probability of exploitation, Electronic support measures

1 Introduction

In the last years, several works in the literature deal with noise radar technology (NRT); among them, there are recent publications such as [1–3], where demonstrator design aspects and field trials are highlighted. In most cases, the research on NRT starts from the assembly of a radar demonstrator, sometimes modifying an existing apparatus exploiting the commercially available advanced hardware and software resources, permitting an easy generation and processing of the random waveforms. However, often little attention has been paid to design noise signals—and related processing—best suited to real applications.

This overview paper—after a brief recall on radar signal processing and on waveforms—is aimed to summarize the advantages and limitations of random waveforms, highlighting that the continuous emission (CE) architecture has to be preferred to the pulsed one. Finally, signal processing for CE noise radar, named range filter bank (RFB), is described pointing out that the RFB grants range/Doppler processing avoiding any unnecessary processing load. The overall scope of this work is to provide indications for passing from some prototype version to an operational noise radar system.

Modern radar signal processing [4] is mostly based on filtering both in *"fast time"*, i.e., by pulse compression along the echo–delay (or range) direction, and in *"slow time"*, i.e.,

by cross-range or Doppler computations in the azimuth direction. In *fast time*, L radar samples are acquired during a pulse repetition interval (*PRI*). Each sample belongs to a different echo–delay and contributes to form the range bins for an assigned direction. In *slow time*, the N consecutive pulses (updated every *PRI*) within the coherent processing interval (*CPI*) are treated for Doppler processing. The overall processing involves N samples in each of the L range bins as shown in Fig. 1a and b. The figures depict the exemplary case of two targets, one (green) staying in each resolution bin and one (red) moving in different resolution bins. The $N \times L$ samples form the data matrix for range/Doppler processing (Fig. 1c). Typical time scales are microseconds for *fast time* and tens to hundreds of milliseconds (up to seconds in synthetic aperture radar (SAR) imaging) for *slow time*.

The moving target detector (*MTD* [5]) is a signal processing architecture able to perform, in the presence of additive white Gaussian noise, the optimal detection of moving targets with radial velocity $v_D = \frac{\lambda}{2} f_D$, being λ the radar wavelength and f_D the frequency shift due to the Doppler effect, as well as to improve the targets detection in ground and in rain clutter. Having acquired N pulses from the target during the dwell time, one can compute the coefficients (impulse response) of the optimal filter which maximizes the signal-to-noise ratio (SNR) or, in clutter areas, the signal-to-clutter ratio [6, 7] according to the Neyman–Pearson theory for the optimal filter.

Since f_D is unknown, to identify the presence of the target it is necessary to use a bank of filters, where the band of the filter ith is in the interval $\left[\left(i-\frac{1}{2}\right)\frac{\mathrm{PRF}}{N}, \left(i+\frac{1}{2}\right)\frac{\mathrm{PRF}}{N}\right]$ for $i=0, 1, \ldots, N-1$ with $\mathrm{PRF} = 1/\mathrm{PRI}$ being the pulse repetition frequency. The optimal solution in white noise leads to a bank of filters implemented via discrete Fourier transform (*DFT*) of the N samples. Figure 2 shows the frequency response of the filter bank overlaying the ideal spectrum (i.e., a *delta* Dirac pulse) of a stationary target and of a moving one.

Due to the finite number of samples, the spectrum of the received signal is not *ideal* and more filters can provide a nonzero output even when noise and interference can be neglected. Moreover, we can consider that the frequency response of a single filter shows side lobes that can affect the target detection.

A new generation of radar transmitters has been developed in the last decades using the solid-state technology. These new transmitters work with peak power levels of two

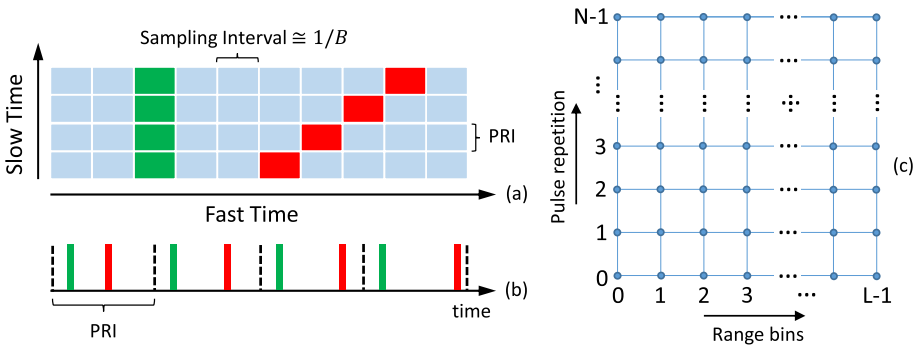

Fig. 1 **a** Slow time/fast time data matrix ($L = 10$ range bins and $N=4$ PRI's). **b** Radar echoes in time of two targets: the first (green) is stationary; the second (red) is moving. **c** A typical data matrix

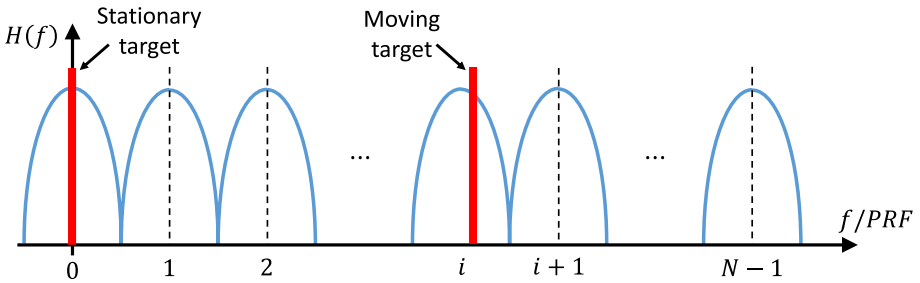

Fig. 2 Frequency response of a bank of filters (DFT) and the ideal spectrum of the useful signal (in red)

orders of magnitude less than cavity magnetrons (and the ensuing power amplifier tubes). The reduced peak power has forced to use long pulses with duty cycles in the order of 10%. Hence, pulse compression techniques are needed to achieve the requested range resolution and to avoid the blind ranges. Pulse compression can be implemented either using deterministic waveforms, the most popular being the frequency-modulated *"chirp"* signal [8, 9], or using random (*noise*) waveforms, as shown in the next section.

2 Radar waveforms

2.1 Deterministic waveforms

Let $g(t) = a(t) \cdot e^{j\phi(t)}$ be the complex envelope of a signal with bandwidth B and duration T. The transmitted signal is modulated both in amplitude (AM) and in phase (PM) by the functions $a(t)$ and $\phi(t)$, respectively. Let us denote by $\phi'(t)$ and $\phi''(t)$ the first and the second derivative of $\phi(t)$. When the time-bandwidth product $B\,T$ *is much greater than* 1, according to the *stationary phase principle* [8, 9] the spectrum of the signal for a given instantaneous frequency $f_t = \frac{1}{2\pi}\phi'(t)$ is approximated by: $\left|S\left(f_t\right)\right|^2 \cong 2\pi \frac{a^2(t)}{|\phi''(t)|}$. Hence, the amplitude $a(t)$ is related both to the spectrum and to the phase $\phi(t)$ by: $a(t) \cong \sqrt{\frac{1}{2\pi}|S(\phi'(t))|^2 \cdot |\phi''(t)|}$. In a linear frequency-modulated (LFM) signal, $\left|\phi''(t)\right|$ is constant and, if also $a(t)$ is constant, the spectrum is approximately uniform (for BT $\gg$ 1) inside the band B, obtaining the widely known *chirp* signal. The autocorrelation function (ACF) of a LFM chirp has a main lobe width of $1/B$ and a side lobe level of 13 dB below the peak, which is too high for many practical applications. To attenuate the sidelobes, it is possible to shape the amplitude of the pulse according to a suited time window [10], leading to some loss in SNR because of the reduced transmitted power due to the amplitude modulation. Moreover, the time window might lead to mismatching losses if weighting is not applied also at the receiver, i.e., if the matched filter is not fully implemented. Another way to lower the sidelobe level of the signal is to maintain a constant amplitude (with full exploitation of the transmitted power) and to pre-distort (i.e. to shape) its frequency law $\phi'(t)$, weighting its spectrum ($\left|\phi''(t)\right|$ being no longer constant). Shaping the frequency law leads then to a nonlinear frequency-modulated signal (NLFM), able to reach very low sidelobe levels (typically less than -40 dB) even when $a(t)$ is kept constant, i.e., when the spectrum is shaped through $\left|\phi''(t)\right|$ only [11]. The historical most famous NLFM signal is the Millett waveform [12], i.e., a *"cosine squared on a pedestal"* weighting, with a theoretical peak sidelobe level of -42 dB for large BT($>$ 1000). When a low BT

is required, as in various applications like air traffic control radar and the last-generation coherent marine (or navigation) radar, the stationary phase principle is no longer applicable. Theoretically, very low sidelobe levels in the ACF can be obtained by a "hybrid" approach, i.e. combining a proper choice of the phase law with a suited amplitude modulation to reduce the SNR loss. Using the hybrid nonlinear frequency-modulated (HNLFM) waveforms [details are found in 13–15], it is possible to attain very low sidelobe levels, less than -60 dB, already for BT $\cong 100$, with very low SNR loss (-0.58 dB only). However, to reach this performance, HNLFM requires high accuracy in the $a(t)$ which is a hardly achievable task if high-power amplification is required.

The examples shown in Figs. 3 and 4 are referred to the illustrative case of a marine/coastal radar operating at X-band (9.3–9.5 GHz) around a central frequency of 9.4 GHz (wavelength of about 3.2 cm). The bandwidth is 50 MHz, with a waveform duration from 2 to 2000 μs (i.e., BT from 10^2 to 10^5). Figure 3 shows the normalized

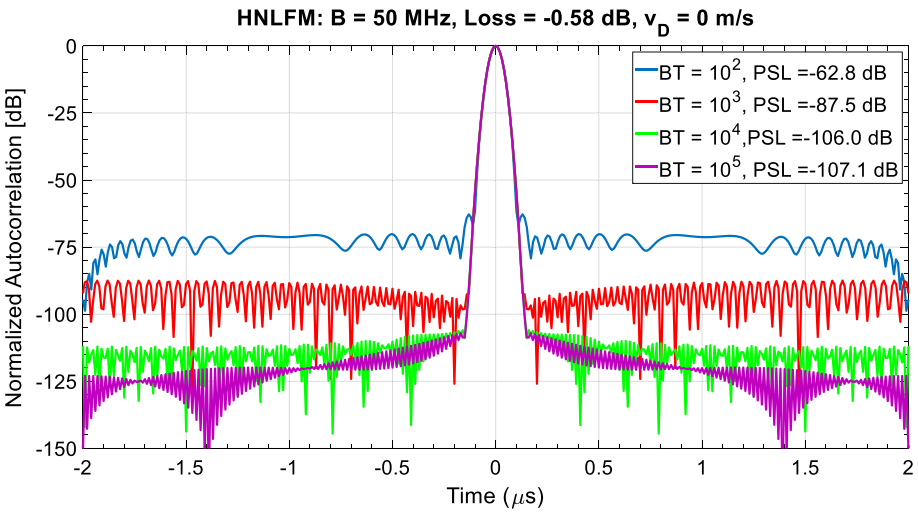

Fig. 3 Normalized ACF in decibel (dB) of a HNLFM waveform with varying BT (no Doppler shift, perfect generation and reception)

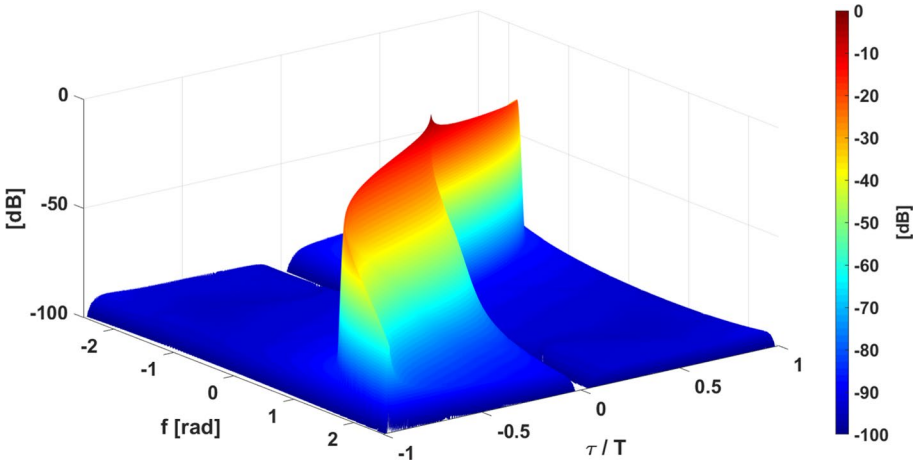

Fig. 4 Ambiguity function of a HNLFM chirp in decibel (dB) below the peak. BT = 1000: delay normalized to the duration *T*, normalized Doppler frequency in radians

ACF of a HNLFM with BT values ranging from 10^2 to 10^5 for a stationary target (i.e., without Doppler shift).

In order to take the radial velocity (i.e., the Doppler effect) into account, it is necessary to introduce the *ambiguity function* (AF) which represents the output of the matched filter when the echo is affected by a Doppler shift f [16, 17]:

$$\mathrm{AF}(\tau,f) = \left| \int_{-\infty}^{+\infty} g^*(t) g(\tau + t) e^{j2\pi ft} dt \right| \tag{1}$$

Figure 4 shows the AF of a HNLFM signal with unit energy and BT = 1000.

For more than 50 years, chirp signals have dominated the radar scenes although many other waveforms have been developed, such as Golomb sequences [18], Barker [19], Frank [20], Costas [21], complementary codes [22, 23] and more [24]. In the frame of frequency-modulated signals, a Costas waveform of length $T = \mathrm{M}t_b$ (with M being an integer) is:

$$g(t) = \frac{1}{\sqrt{\mathrm{M}t_b}} \sum_{m=1}^{M} \exp\left(j2\pi f_m t\right) \cdot \mathrm{rect}_{t_b}\left[t - (m-1)t_b + \frac{T}{2}\right] \tag{2}$$

It is obtained dividing the time–frequency plane in M sub-elements (chips) of equal duration t_b (chip time) and band $\Delta f = \frac{1}{t_b}$ with $f_m = a_m \Delta f$ $(m = 1, 2, \ldots, M)$ the carrier frequency of the mth chip. The code is defined by $a = [a_1, a_2, \ldots, a_M]$, the sequence of integers between 1 and M (*hopping sequence*, Fig. 5). In Eq. (2), $\mathrm{rect}_{t_b}(t)$ is equal to 1 for $0 \le t < t_b$ and *zero* elsewhere. The band of the Costas signal is $B = M \cdot \Delta f$, and the compression ratio is M^2.

Figure 6 shows the ambiguity function of a Costas code with $M = 40$ and $T = 16$ μs (BT = 1600) having unit energy. A drawback of these codes is the limited number of available waveforms.

Generalizing this type of waveforms, the need for low probability of intercept (LPI) radar has pushed the *"randomization"* of the transmitted frequency (and sometimes of the pulse repetition interval) of military radar since the WWII [25], leading to *"frequency agile"* and *"random PRT stagger"* operation [26]. The pertaining ambiguity function has been mathematically analyzed in [27].

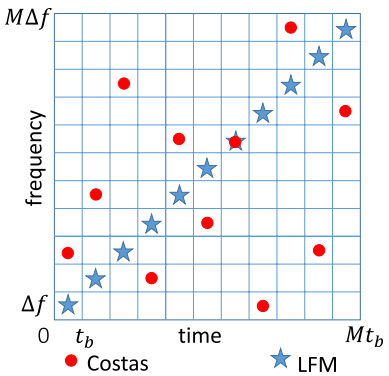

Fig. 5 Costas code: frequency hopping compared with the LFM waveform

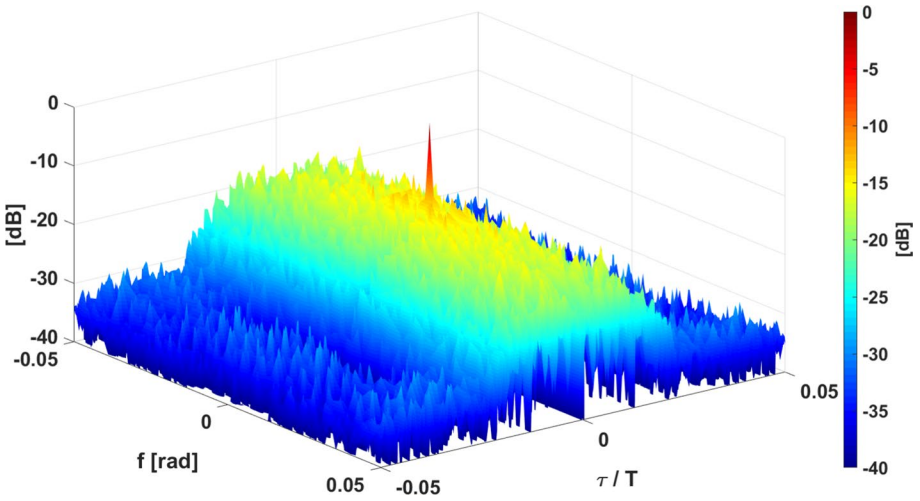

Fig. 6 Ambiguity function in decibel (dB) of a Costas waveform, BT = 1600

Summing up, all the classical deterministic radar waveforms, used since the early days of radar, have intrinsic problems: high sidelobe level for high Doppler shifts and/or limited availability of orthogonal modulations (implemented as *"up"* and *"down"* direction of the frequency modulation in LFM/NLFM/HNLFM chirps) that make them suited to defined applications.

In principle, *noise* (random) waveforms, as analyzed in the following, do not suffer from the above disadvantages since, by definition, they have a *"thumbtack-like"* ambiguity function without the need for a complex generation algorithm. Moreover, being each waveform a single realization of an endless random process, their number is theoretically unlimited.

Finally, we believe the bank of Doppler filters to be the best solution for range–Doppler processing in noise radar surveillance, similar to the well-known and widely used moving target detector.

Considering the intrinsically low Doppler tolerance of the random codes used in all noise radars, a bank of Doppler filters is best solution for range/Doppler processing for the surveillance function using NRT. This approach is called range filter bank (see Sect. 6.3) and extends the widely used moving target detector to NRT.

2.2 Pseudo-random waveforms

In noise radar technology (NRT), the transmitted signals are random or, strictly speaking, *pseudo-random* waveforms (i.e., realizations of a random process) and theoretically uncorrelated with each other.

Since the 2000s, the advancement of technology has offered the ability to produce and process noise waveforms using modern computation elements and high-speed analog-to-digital (ADCs) and digital-to-analog (DACs) converters. Along with FPGAs (field-programmable gate arrays), these building blocks permit the generation of high-performance digital noise waveforms. The digitalization of the radar signal generation and processing allows us to design waveforms with novel approaches, driven by signal processing principles rather than by the capabilities of the hardware. However, one

must remember what Cook and Bernfeld stated [28]: *"in the extreme case, all signals (waveforms) are equally good (or bad) as long as they are not compared against a specific radar environment."* Hence, it is very important for the waveform radar designer to know where the radar is going to operate and which requirements are needed for the specific application. This suggests that NRT is a powerful tool when it is *"tailored"* to the specific need, but, of course, that no single waveform (including NRT) is to be considered a kind of *universal solver*.

Concerning the *"randomness"* of the NRT waveforms, while in principle it is possible to use an analog noise generator [29], most recent trends rely on more effective and manageable pseudo-random number (PRN's) generators [30, 31].

2.3 Advantages of random waveforms

There are three main advantages of noise waveforms in comparison with the deterministic ones: first, a desirable ambiguity function, i.e., a *"thumbtack-like"* one, able to guarantee high range/Doppler resolution and the absence of range–Doppler coupling; second, the potential for coexistence with other radars and/or other sources, thanks to the possibility to generate a very large number of *orthogonal* waveforms; finally, the possibility to design waveforms with low probability of intercept and exploitation (LPI/LPE) features [32].

2.3.1 Ambiguity function

A realization of an infinitely long (B and T both tending to infinity) *"white noise"* has an AF going to a *delta* Dirac function, hence with a level of ambiguity decreasing with BT increasing. However, in real applications both B and T are limited, and the peak side level (PSL) of the AF has a fluctuating value with a mean value close to the *"processing gain"* BT (see Sect. 2.4.1). Figure 7 shows the exemplary ambiguity function of a noise waveform with unit energy and BT = 1000.

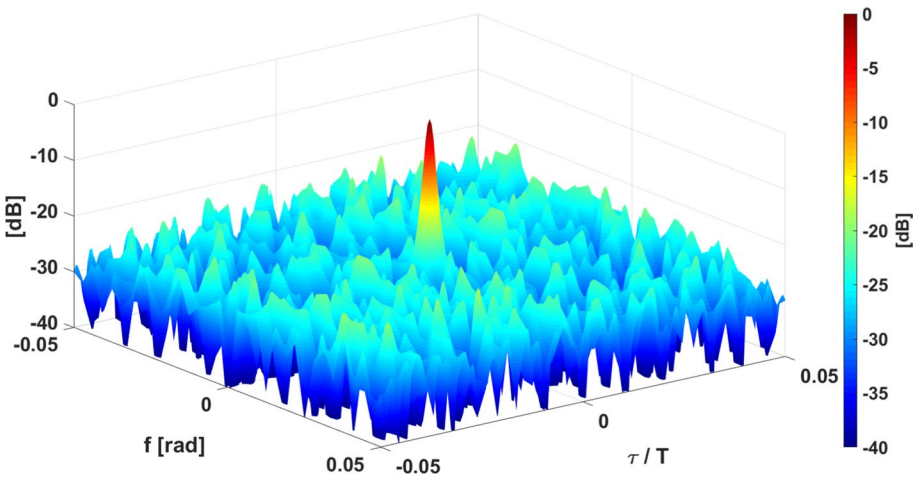

Fig. 7 Ambiguity function in decibel (dB) of a noise waveform. BT = 1000

2.3.2 Coexistence with other radars and other sources

The increasing scarcity of the electromagnetic spectrum (which forms the basic, non-renewable resource for radio communications, radio navigation and radar) calls for an organized coexistence of the radio-based services. This issue might be addressed by the communication and radar spectrum sharing (CRSS), a complicated problem, whose practical solution, today, can be based on the use of artificial intelligence (AI) with its machine learning/deep learning tools [33]. Moreover, orthogonality between waveforms plays a fundamental role in many applications, particularly in MIMO (multiple-input, multiple-output) radars [34] and, potentially, in modern civil marine radars [35]. Novel modulations for marine radars are needed, mainly to improve the spectral efficiency and to allow continuous operation of multiple radars with solid-state transmitters in the same frequency band and in the same marine area [35]. Using NRT, mutual interferences to/from many radars located in the same area and operating in the same limited frequency band are reduced.

Equation (3) defines the cross-ambiguity function (CAF) between two signals $g(t)$ and $s(t)$:

$$\mathrm{CAF}(\tau, f) = \left| \int_{-\infty}^{+\infty} g^*(t) s(\tau + t) e^{j2\pi f t} dt \right| \tag{3}$$

For zero-Doppler (i.e., $f = 0$), Eq. (3) becomes the cross-correlation function (CCF), which can be used to evaluate the orthogonality between two waveforms. Figure 8 compares the ACF (in blue) of a noise waveform with the CCF (in red) of two noise waveforms with the same bandwidth and duration (BT = 1000). In the sidelobes region, both curves show a similar behavior.

2.3.3 Low probability of intercept and of exploitation

The acronym LPI (low probability of intercept [32]) indicates the feature of a radar to make difficult its detection by an opponent using means of passive interception such as electronic support (ES), radar warning receivers (RWR), or electronic intelligence (ELINT) receivers

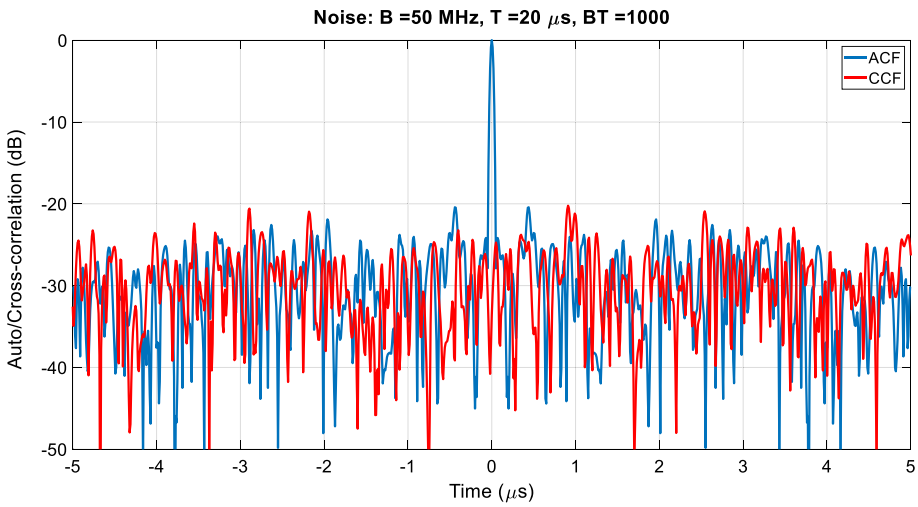

Fig. 8 ACF and CCF between two exemplary noise waveforms: $B = 50$ MHz, $T = 20$ μs

with the final aim to create a suited radar jamming. Today, both electronic warfare (EW) [36–46] and radar systems are exploiting more and more *"intelligence"* thanks to the convergence of computer science, big data analysis and communications.

There are many methods in the literature for intercepting LPI radars. In [47, 48], filter banks with higher-order statistics and wavelet transform are proposed. Some methods are based on time–frequency transforms such as short-time Fourier transform and Wigner–Ville transform [49, 50]. In [51], quadrature mirror filter banks are used, while [52] uses cyclostationary processing. An innovative method is described in [53] and [54], based on the use of two receivers on board of a fast-moving platform (e.g., an airplane or a satellite). Recently, a new waveform recognition technique (WRT), based on a convolutional neural network (CNN), has been proposed in [55].

In the frame of a specific emitter identification (SEI) capability in modern ES/ELINT systems [56] introduces a classification technique based on some suitable features evaluated from the cumulants of the signal emitted by the radar system.

Noise radar is probably a very effective answer to the increasing demand for operational LPI radars [32], a feature that improves if coupled with low power, wide bandwidth, frequency variability, or other suited design attributes. As a matter of fact, modern interception methods such as the two-antenna correlation receiver [57], seems effective against sophisticated radar waveforms including the pseudo-random ones.

2.4 Limitations of random waveforms

There are two main limitations when using noise waveforms: First, the peaks of the side lobes in the autocorrelation function are random with a mean value related to the product BT [1]. Second, the scarce exploitation of the power amplifier when the peak-to-average power ratio (PAPR) is significantly greater than the unity.

2.4.1 Random sidelobes and peak sidelobe level

For a noise waveform $g(t)$ of duration T and bandwidth B, the correlation processing (matched filtering) generates random fluctuations in the peak sidelobes level (PSL) of the ACF; see Fig. 9. Normally, a delay τ^* divides the time axis into two parts (in Fig. 9, $\tau^* \cong 0.1$ μs). It is defined as follows: For delay less than τ^*, all different realizations of the ACF are very close to each other both in the main lobe and in the first sidelobes. When the delay is greater than τ^* (i.e., in the *"random sidelobes region"*), the sample mean of the ACF converges to the theoretical mean $\sqrt{\frac{\pi}{4\mathrm{BT}}}$, as shown in [1], where the distribution of the PSL has been deduced, which permits to estimate a PSL level, that is not exceeded for a given probability δ. Such a level depends on the product BT and on the particular type of noise spectrum. It can be estimated as:

$$\mathrm{PSL}_{\mathrm{dB}} = -10 \cdot \log_{10}(\mathrm{BT}) + K \tag{4}$$

where K is a constant, typically in the range 10–13 dB, depending on the chosen probability δ, as shown in Fig. 10 for different values of BT.

2.4.2 Limited exploitation of the power amplifier

In the design of noise radar waveforms, in addition to the bandwidth B and duration T, another relevant parameter is the peak-to-average power ratio (PAPR), i.e., the

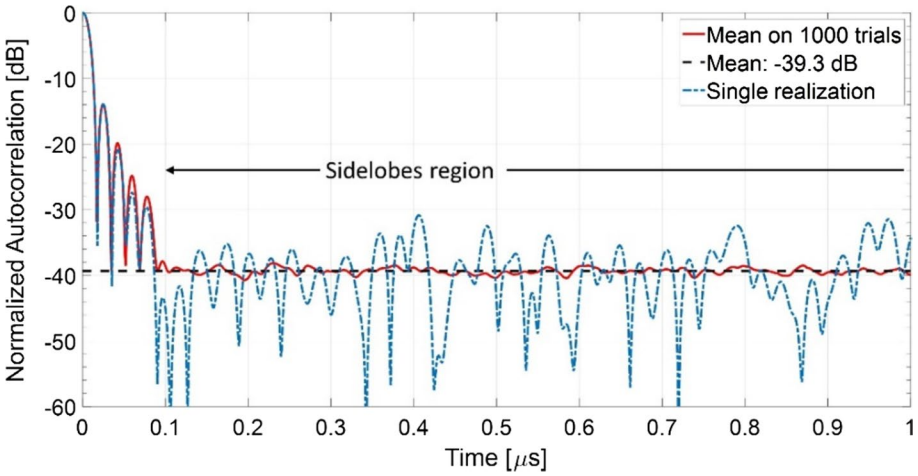

Fig. 9 Normalized ACF of an exemplary noise waveform with uniform power spectrum ($B = 50$ MHz, $T = 109$ μs). Comparison between a single realization (blue), the sample mean on 1000 trials (red) and the mean value (black) in the sidelobes region($t \cong 0.1$ μs)

ratio $\frac{\max\limits_{k} |g[k]|^2}{\frac{1}{N}\sum_{k=1}^{N} |g[k]|^2}$ where $g[k]$, with $k = 1, 2, \ldots, N$, are the samples of the signal taken at the Nyquist (or smaller) interval.

Normally, deterministic waveforms (chirp, Barker, polyphase codes, etc.) have unitary PAPR (i.e., the signals are *"unimodular"* with phase or frequency modulation), while an arbitrary noise waveform (unless hard-limited) has a PAPR greater than one with a maximum (said *"natural"* PAPR in the following) around 10.5 to 12.5 for a probability $\delta = 0.01$ and BT between 10^3 and 10^6; see Fig. 10. In this situation, the power transmitter is less efficient than one that could work in saturation; hence, a loss in SNR arises equal to $-10 \cdot \log_{10}$ (PAPR) [dB]. Figure 11 shows this loss versus the PAPR.

Of course, the advantage to use *unimodular* noise signals (PAPR = 1) is the absence of such a loss, while the drawback is that the number of degrees of freedom of the

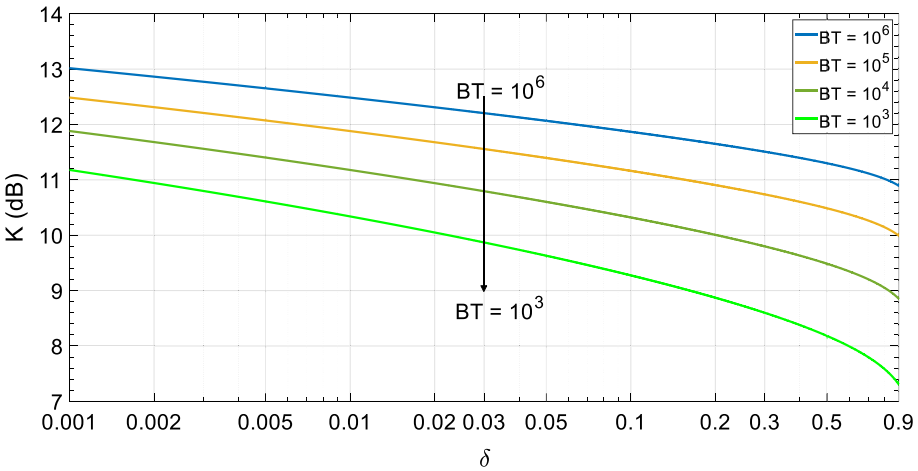

Fig. 10 Parameter K (dB) in Eq. (4) versus the probability δ with BT varying, [1]

waveform is halved, passing from $2BT$ real degrees of freedom (amplitude and phase pairs, or real and imaginary parts of the signal) to BT.

This point is important in the identification and exploitation of the signal and calls for a trade-off between the transmitted power exploitation, the number of degrees of freedom and the PAPR.

2.5 Trade-off related to the peak-to-average power ratio

As shown in the previous section, for a noise waveform the *"natural"* PAPR is around 10–12 implying some high loss in SNR (order of -10 dB, see Fig. 11). To reduce this loss, the PAPR can be forced, using a suited nonlinear waveform transformation, to a much lower value (e.g., to PAPR$=1.5$ which reduces the loss to -1.76 dB only). An algorithm, called *"Alternating Projection"* [58], forms a robust and computationally efficient method to control the PAPR and to design waveforms with given structural properties [59].

However, a nonlinear transformation aimed to the PAPR reduction modifies the underlying random process and destroys its original Gaussian statistics. To measure the distance of a zero-mean random variable X of variance σ^2 from the Gaussian one, the *negentropy* $J(X)$ is used [60]:

$$J(X) = h_G(X) - h(X) \tag{5}$$

where $h_G(X) = \frac{1}{2}\ln\left(2\pi e\sigma^2\right)$ is the *entropy* of a Gaussian random variable of variance σ^2. It is well known that the Gaussian has the maximum entropy among all distributions with the same variance. Then, $J(X) > 0$ is a measure of the *distance* of X from the Gaussian distribution.

Often, the evaluation of the negentropy is very difficult when the probability density function is unknown. Figure 12 shows the estimated negentropy of the real part of a single noise waveform with uniform spectrum ($B=50$ MHz, $\sigma^2 = 0.5$) varying the PAPR, where $h_G(X) = \ln\left(\sqrt{\pi e}\right) \cong 1.0724$, while $h(X)$ is estimated using the histogram approximation of the probability density function. With the PAPR decreasing up to a value of $4\sigma \cong 2.8$, the underlying process *"starts"* to be non-Gaussian, and the SNR loss also decreases (Fig. 11), i.e., the loss of Gaussianity is the price paid for the transmitted power efficiency.

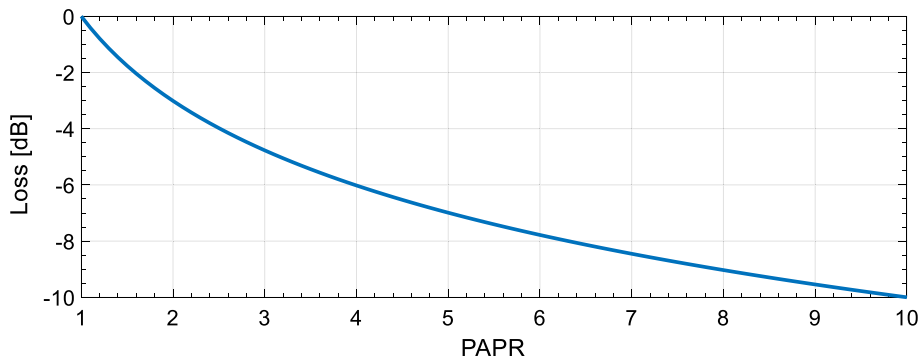

Fig. 11 SNR loss (dB) versus the PAPR

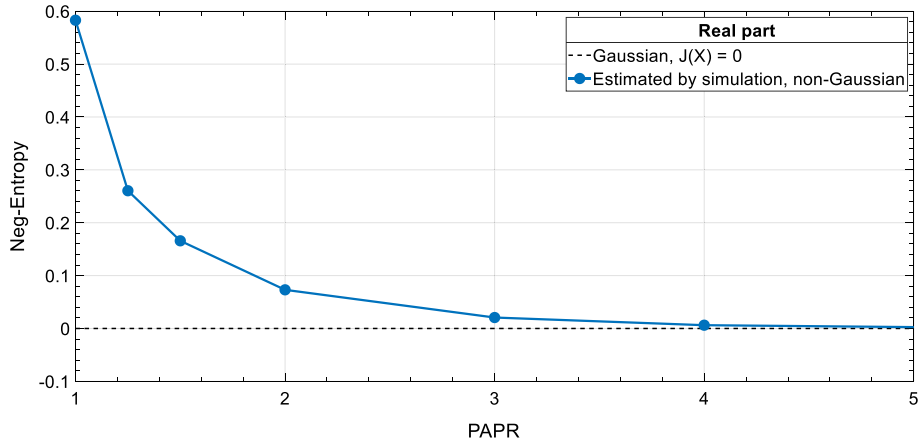

Fig. 12 Negentropy, Eq. (5), versus PAPR of the real part of a single noise waveform with unit power and uniform spectrum

3 Historical overview of noise radar technology

Noise radar was introduced for the first time in 1959 by Horton for a system able to measure the distance of a target [61]. Historically, the generation of noise signals was first implemented using analog sources [62]. For instance, in the 1990s, methods for an efficient generation of *"chaotic"* signals from an analog source at W-band were developed and tested in Ukraine [29, 63]. In China, studies of random signals radar (RSR) date back to the 1990s; they concerned the design of noise FM-CW radar and its implementation for collision warning of vehicles and for battlefield surveillance [64, 65]. In the USA, at the end of 1990s, noise radar technology was applied to design a coherent ultra wide-band (UWB) random noise system for Doppler estimation [66, 67] and airborne imaging [68], and a new technique for the range sidelobe suppression of UWB random noise radar was proposed and analyzed. Since the early 2000s, a constant, experimental research activity with numerous field trials takes place in Ukraine, where in 2002, the First International Workshop on Noise Radar Technology (NRTW 2002) was held [69, 70]. Theoretical analysis was developed in [71–73] regarding noise radar using random phase/frequency modulation. Concerning the analysis carried out in [72, 73], it has to be noticed [74] that a main drawback (which seems to *"propagate"* among different researchers) is the wrong assumption that the phase $\theta(t)$ is a Gaussian random process, neglecting the fact that the phase is folded in the range $-\pi$ to $+\pi$.

In Poland, at the Warsaw University of Technology, a noise radar demonstrator was implemented (starting from 2010 and using commercial hardware) for the detection of moving targets at short ranges. The signal processing included adaptive filtering for clutter removal. The processing was validated with real-life experiments, during which cars at ranges of hundreds of meters and aircraft at ranges of a few kilometers were detected [75]. During the experiments, the main drawback was the occurrence of the masking effect (i.e., a weak target is masked by the sidelobes of a strong one). Hence, in [76], a filter-based method was introduced to create noise-like waveforms with very low sidelobes in certain range and Doppler intervals, and more publications followed.

From 2005, a considerable effort on NRT pre-competitive and unclassified research is being developed in the frame of the NATO Science and Technology Organization

(STO) Research Task Groups (RTG's). The related results until 2018 are described in the official reports of RTG SET-101 "Noise Radar Technology" (2005–2008), RTG SET-184 "Capabilities of Noise Radar" (2012–2014) and RTG SET-225 "Spatial and Waveform Diverse Noise Radar" (2015–2018). From December 2020, the RTG SET-287 "Characterization of Noise Radar" is active. In SET-101 and SET-184, the objectives were to identify the areas where noise radar would provide significant advantages over the classical radar. The conclusions were an evaluation of architectures, technologies and components for the development of noise radar technology with emphasis on implementation of software-defined radar, pseudo-random waveforms design/generation and radar returns processing using arbitrary waveform generators (AWG), FPGA-based signal processing and multicore/parallel computing. In SET-184, it was shown that noise radar technology is capable of providing new electronic protection capabilities to short-range operational tactical radars [77–79]. In SET-225, it was demonstrated that noise radars can be developed to fulfill useful military applications. This was done by cooperatively building and field testing two radar transportable demonstrators at the Fraunhofer FHR Institute in Wachtberg (Germany) and at the Turkish Naval Research Center Command (TNRCC) in Istanbul (Turkey), respectively. In the summer of 2018, field trials of the first demonstrator were held at the FHR site in Wachtberg [80]. Both static targets (corner reflectors) and moving targets (cars, aircraft) have been used to check detection capabilities in the presence of clutter, multipath and antennas' coupling, as well as to test radar resolution. The TNRCC demonstrator was tested in the coastal environment of Marmara Sea (Turkey) [81]. In both sets of field trials, the importance of the range sidelobes from close-in targets and from the transmit–receive leakage in affecting the practical sensitivity of the radar has been clearly highlighted. A large amount of work, that has been carried out by the members of the NATO groups, particularly SET-225, is described in [2].

Active since December 2020, the unclassified RTG SET-287 "Characterization of Noise Radar" aims to produce recommendations for the specification and characterization of noise radars. The main topics of this research are the following:

- Control and characterization of direct leakage between transmitter and receiver.
- Control of sensitivity floor due to range sidelobes of large targets.
- Minimization of transmitter power consumption and processing load.
- Development of low probability of intercept (LPI) and interference rejection features.
- Effective use of RF spectrum by exploiting the flexibility of transmitted waveforms.

In this frame, the evolution of the previously introduced demonstrators was tested in different (land and marine) environments showing their suitability for short-range, high-resolution surveillance [3]. The experiments confirmed the need for tailoring the transmitted waveform to improve the receiver dynamic range and to counteract the damaging effects of leakage and of nearby clutter and strong targets.

The interested reader can find a signal processing viewpoint introduction to noise radar, in [82], while an overview of the Italian academic contribution to radar (and to NRT) is available in [83].

4 Noise radar architectures

The basic elements of many noise radar designs are similar. In the preferred, continuous emission (CE) architecture, the transmission and the reception channels are implemented with a specified mutual isolation to avoid leakage due to antenna coupling as shown in Fig. 13. To reduce the damaging leakage on target detection, in principle there are three possible approaches: first, acting on the apparatus, i.e., increasing the antenna isolation (the state of the art for co-located antennas, X-band, is around 90 dB); second, using adaptive power cancellers; and third, acting on the transmitted waveform generator, i.e., improving the peak to sidelobes level PSL.

Figure 14 shows a simple block diagram of a continuous emission noise radar, where a general functional separation into a digital back end and an analog front end is shown. The front end has the simple function to convert the radar signals between an intermediate frequency (IF) band and a desired radio frequency (RF) band. The ports of the front end are labeled by S (*received* or *surveillance* signal), W (waveform), RX and TX. Let us consider the transitions between these ports. The up-conversion is performed from port W, the waveform input, to the transmitting antenna at port TX. The back end embodies most of the typical CE noise radar functionalities, including the correlation (more generally, the cross-ambiguity function (CAF)) of the received signal with the pertaining

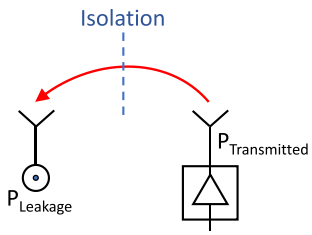

Fig. 13 Leakage due to the antenna coupling

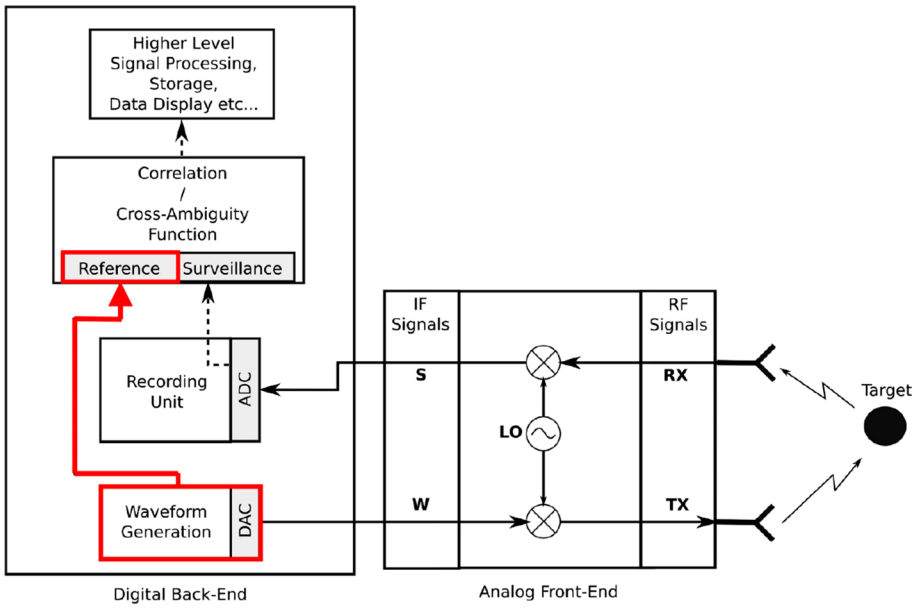

Fig. 14 Block diagram of a continuous emission noise radar. Solution (a): the reference is the digital record of the transmitted code

reference. The latter represents a replica of the transmitted waveform, and its acquisition distinguishes two basic approaches: solution (a) of Fig. 14 and solution (b) of Fig. 15.

Solution (a) is the simplest implementation of a CE noise radar, which obtains the reference signal from a digital copy of the waveform samples that are provided to the digital-to-analog converter (DAC). Its advantage is the simple RF front end. Its drawback is that the reference signal might deviate from the actual transmission when the all-digital reference acquisition does not respect the transfer function of the front end. Consequently, Fig. 15 shows the alternative approach, where a coupler from the RF transmission path supplies the reference signal which is down-converted along with the surveillance signal and digitized by a separate analog-to-digital converter (ADC).

This implementation, with the cost of an ADC, an additional channel signal to the additional front-end port R, delivers a more robust reference signal and, more important, makes the waveform generation independent of the implementation of the signal processing. In fact, the waveform might be created by any source, not necessarily digital, complying with the signal specifications of the port *W*, where the reference signal is acquired by the front end.

5 Waveforms design

In NRT, the transmitted signal could be derived from physical phenomena, as *thermal noise* in amplifiers or Zener diodes [29]. However, this approach is often impractical due to accuracy, resolution and dynamic range limitations. Hence, digital implementation, as in most cryptographic applications, is preferred. In this frame, the design of noise waveforms is based on the computer generation of sequences of pseudo-random numbers (PRNs). Starting from an initial value, called *"seed"*, which defines the whole sequence, when the *machine* returns to the initial point, the sequence repeats

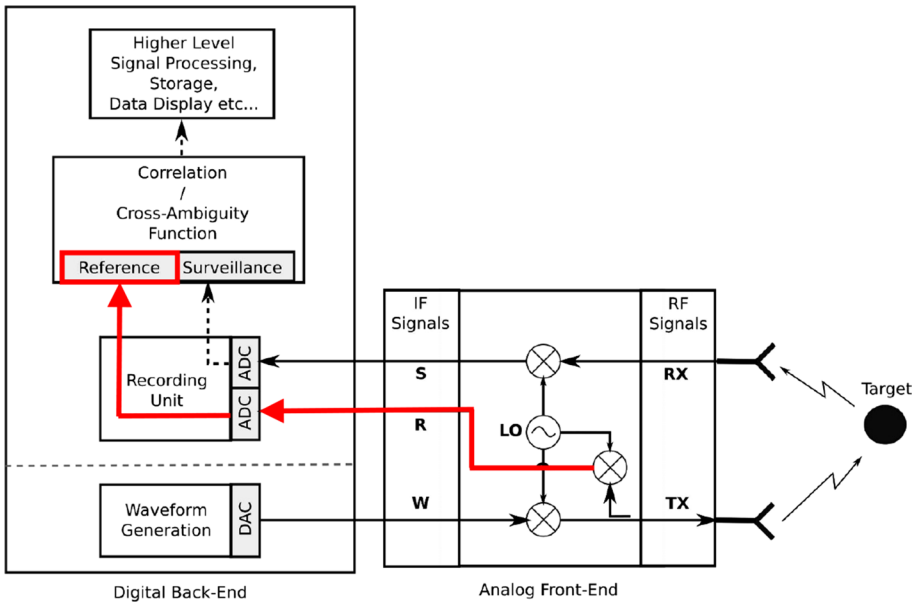

Fig. 15 Block diagram of a continuous emission noise radar. Solution (b): the reference is the record of the transmitted signal at the antenna port

itself. Therefore, one should speak of pseudo-randomness, meaning that these numbers *appear random* to an external observer as they pass some statistical tests [84].

The aforementioned periodicity problem is made immaterial by generation algorithms such as the "Mersenne Twister" [30], a family of PRNGs (pseudo-random number generators) based on F2-linear maps [85], whose period is the huge $2^{19937} - 1$ for 32-bit integers. In practice, the period of the sequence is a minor problem with respect to the low statistical quality of some widely used PRNGs [86].

For constant amplitude noise signals (PAPR = 1), a simple way to generate noise waveforms is to introduce the randomness into the phase (or frequency) as previously discussed [71, 72]. In [87, 88], noise signals are generated adding noise to the well-known deterministic LFM chirp signals. In [89], starting from the classical approach shown in [90], waveforms are generated using a white Gaussian process with its independent, identically distributed (IID) in-phase (I) and in-quadrature (Q) components which is filtered (spectral shaping) in the requested frequency band. To reduce the PSL [91] and to control the spectral width, an iterative algorithm has been proposed in [92] starting from a zero-mean white complex Gaussian process to be band limited in the frequency domain (FFT) by a low-pass filter, then by IFFT normalized (amplitude limited) in the time domain. Iterating this time/frequency projection, the PSL, after some tens of iterations, converges to a minimum. Figure 16 shows a block diagram of a digital noise generator including the PAPR control and the sidelobes suppression in a specific radar range interval [1].

Setting the duration T of the noise waveform and the sampling frequency F_s, the steps are:

(i) A PRNG generates $F_s \cdot T$ independent and identically distributed Gaussian pairs of samples to form the complex sequence with *uniform* spectrum. By filtering with $H(f) = \sqrt{S(f)}$, the initial power density spectrum is *"shaped"* as $S(f)$ inside the band B. The number of independent real samples $2BT$ represents the *"degrees of freedom"* of the waveform.

(ii) The PAPR control block sets, by the alternating projection algorithm [58], the PAPR to a desired value (note that before the spectral shaping, the PAPR has its *"natural value"* of 10–12 or greater). Normally, the PAPR is forced to lower values (e.g., in the range 1.5–2.0), to reduce the SNR loss typically below 3 dB (see Fig. 11). The output is the signal $g_1(t)$, see Fig. 16, i.e., a non-Gaussian sequence with the assigned PAPR.

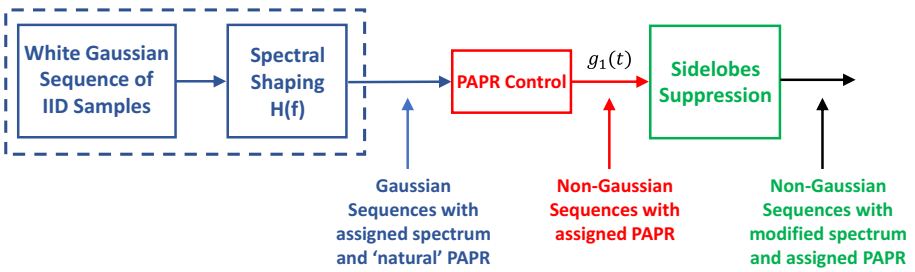

Fig. 16 Block diagram of a digital noise generator with PAPR control and sidelobes suppression

(iii) The sidelobes suppression function improves the PSL in a specific range interval, as shown in Fig. 17a. This method is based on the *inverse filtering* approach (well known in the literature [93]) applied in Fig. 17b to the signal $g_n(t)$. Due to the folding of the spectral components into $\left(-B/2, +B/2\right)$, the output must be iteratively processed by the algorithm (see Fig. 17c, starting from $n = 1$ up to n_{iter}) to obtain the desired range zone suppression.

The *"tailored"* signal at the end of the procedure is used as transmitted waveform.

In [94], a different approach is proposed, called COSPAR (combined spectral shaping and peak-to-average power ratio reduction). It uses a pseudo-random sequence θ of *Uniform* in $(-\pi, +\pi)$ phases to generate the noise waveform. In the frequency domain, the term $e^{j\theta}$ multiplies the square root of the desired spectral density S (see Fig. 18).

Being the length of sequence, normally much greater than one, applying the central limit theorem to the IFFT of $Z = \sqrt{S} \cdot e^{j\theta}$, this transformation makes the components I and Q Gaussian-distributed in the time domain. The peculiarity of this method is that all pseudo-random sequences have the same (deterministic) power spectrum S, chosen so that the autocorrelation function has a deterministic PSL. In [94], the autocorrelation function comes from a Taylor window with 50 dB of PSL (all sidelobes having the same PSL).

6 Signal processing in CE noise radar

6.1 Loss in the optimal processing

Let $g(t)$ be the transmitted radar signal, i.e., a pseudo-random waveform of duration T (often called coherent processing interval—CPI) and bandwidth B around the central frequency f_0, and the received echo signal $s(t)$, a delayed copy of the transmitted signal modulated by the Doppler frequency f, respectively. The digital record of $g(t)$ is the input to the *reference* channel, while the digital record of $s(t)$ is the input to the *surveillance* channel of the radar processor (see Figs. 14 and 15).

The optimum receiver (matched filtering), for a given pair of delay τ and Doppler frequency f, has the well-known non-casual impulse response $h(t) = g^*(-t) \cdot e^{-j2\pi ft}$ the output being the convolution between $h(t)$ and $s(t)$, whose amplitude is the well-known CAF, Eq. (3), that, for $s(t) = g(t)$, equals the AF of the transmitted signal, Eq. (1).

In practice, the durations of the surveillance and reference signals are both finite, equal or less than the *CPI*. Introducing the rectangular window $p_T(t)$, i.e., a unit pulse of duration T, the output $Y_T\left(\tau, f\right)$ of the matched filter is a random process, whose expected amplitude is [95]:

$$\left|E\left\{Y_T\left(\tau, f\right)\right\}\right| = \left|R_{\text{sg}}(\tau)\right| \cdot \text{AF}_{p_T}\left(\tau, f\right) \tag{6}$$

with $R_{\text{sg}}(\tau)$ the cross-correlation function between the random processes $s(t)$ and $g(t)$, while $\text{AF}_{p_T}\left(\tau, f\right)$ is the ambiguity function of $p_T(t)$. For zero-Doppler, the energy of the received signal is $E_T = R_{sg}(0) \cdot T$, that is fully recovered at a near zero distance. Increasing the delay τ in Eq. (6), the finite duration of $p_T(t)$ causes a loss $L_R = 10 \cdot \log_{10}\left(1 - \frac{\tau}{T}\right)$ in [dB]. Note that L_R is negligible when $T \gg \tau$, with $\tau = 2R/c$ and R the distance of the target of interest.

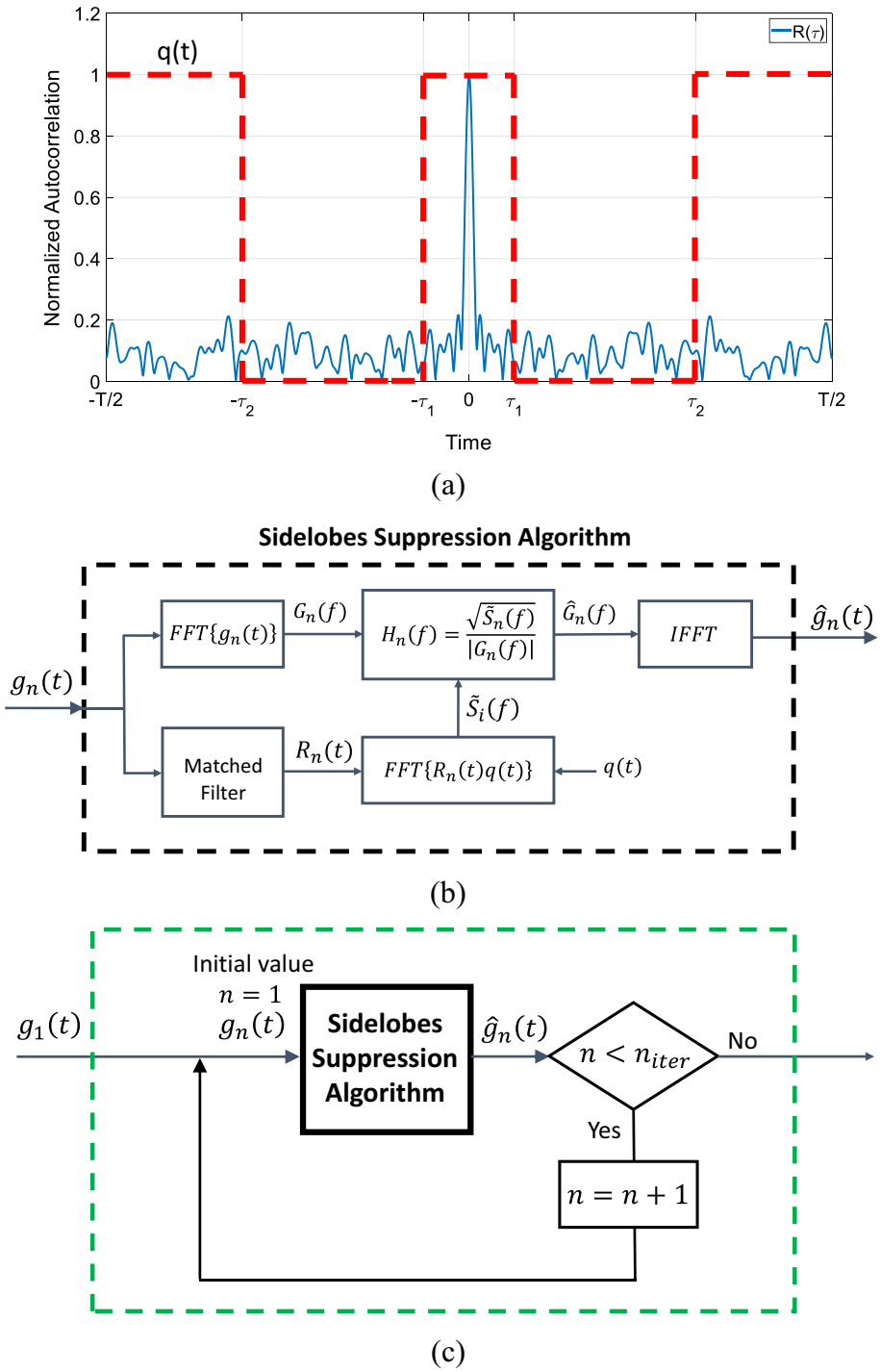

Fig. 17 **a** The sidelobes suppression interval (τ_1, τ_2) as defined by $q(t)$. **b** The inverse filtering method to suppress the sidelobes in a specific range zone. **c** The iterative algorithm to improve the suppression of the sidelobes

At zero-delay, a moving target with radial velocity $v \neq 0$ produces a Doppler shift $f \neq 0$, which causes a loss $L_D = 10 \cdot \log_{10} \left\{ \left| \frac{\sin(\pi f T)}{\pi f T} \right| \right\}$ in [dB].

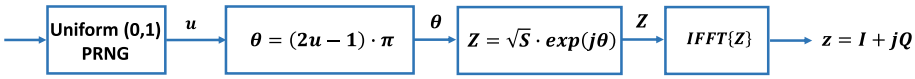

Fig. 18 The COSPAR generator

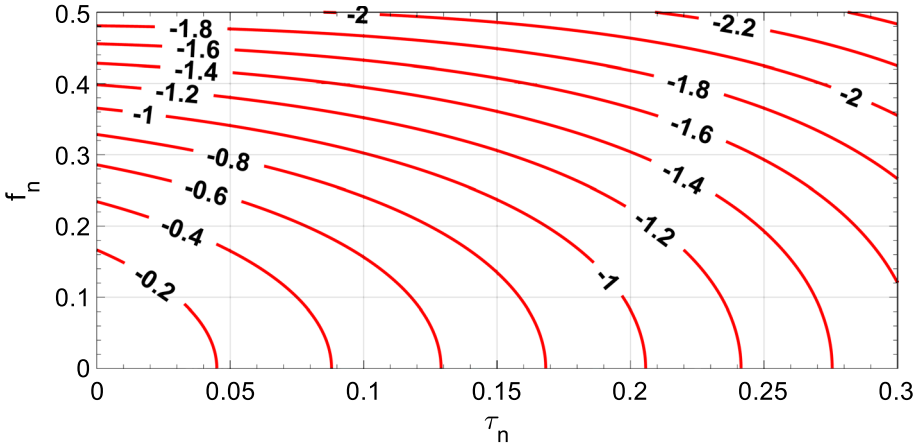

Fig. 19 Losses [dB] due to normalized delay τ_n and Doppler frequency f_n

Combining the delay and frequency effects $(\tau \neq 0, f \neq 0)$, normalizing the time and the frequency axis, i.e., using $\tau_n = \tau/T$ and $f_n = fT$, the loss in [dB] is equal to: $L = 10 \cdot \log_{10}\{|\mathrm{AF}_{p_T}(\tau_n, f_n)|\}$. Figure 19 shows L with (τ_n, f_n) varying. For $\tau_n < 0.1$ and $f_n < 0.25$, the loss may be neglected (being less than -0.8 dB).

6.2 Some considerations on the implementation of the correlation filter

To guarantee a high processing gain BT, the duration T is in the order of the *CPI*, i.e., in the typical range of 10–20 ms. Hence, T results much greater than $\tau_{\max}$, i.e., the delay pertaining to the maximum expected distance, and in the evaluation of the CAF, Eq. (3), a large amount of immaterial data, beyond the maximum range of interest $R_{\max} = \frac{c \cdot \tau_{\max}}{2}$ ($c = 3 \cdot 10^8$ m/s), significantly increases the processing load. If the *CPI* is divided into P contiguous sub-intervals T_r (i.e., one sets $T = P \cdot T_r$), the reference and surveillance signals can be written as: $g(t) = \sum_{p=0}^{P-1} g_p(t)$ and $s(t) = \sum_{p=0}^{P-1} s_p(t)$, where $g_p(t)$ and $s_p(t)$ are the signals in each sub-interval p. At zero-Doppler, $R_{\mathrm{sg}}(\tau)$ is:

$$R_{\mathrm{sg}}(\tau) = \sum_{p=0}^{P-1} s_p(t) \otimes g_p(t) + \sum_{i=0}^{P-1} \sum_{\substack{j=0 \\ i \neq j}}^{P-1} s_i(t) \otimes g_j(t), \quad 0 \leq t \leq 2\mathrm{PT}_r \tag{7}$$

where $\otimes$ denotes the correlation operator. The envelope of $|R_{\mathrm{sg}}(\tau)|$ is the well-known triangle of base $2\mathrm{PT}_r$ and height PT_r. Note that for the delay $\tau_{\max}$ of the farthest target, it results $\tau_{\max} \ll T$ and we can set $\tau_{\max} = M \cdot T_r$, where the duration T_r is short enough to make the related Doppler shift negligible along the time T_r and the integer M is such that the maximum range of interest (distance of the farthest expected target) is $\mathrm{cMT}_r/2$. Imposing a maximum Doppler shift of $\Delta\varphi = 2\pi f T_r < \frac{\pi}{16}$, the maximum T_r is equal to

Table 1 T_r for different moving targets (X-band)

Moving target	Doppler velocity v	T_r
Ship	25 m/s (50 knots)	$\cong$ 20 μs
Land vehicle	70 m/s (250 km/h)	$\cong$ 7 μs
Civil aircraft	250 m/s (900 km/h)	$\cong$ 2 μs
Military aircraft	1000 m/s (Mach 3)	$\cong$ 0.5 μs

$\frac{1}{32 \cdot f} = \frac{\lambda}{64 \cdot v}$ where v is the maximum radial speed (Doppler velocity) of interest. At X-band ($\lambda = 0.032$ m), Table 1 shows possible values of T_r for different Doppler velocities of the target.

6.3 Range Filter Bank (RFB)

The aim of the algorithm named range filter bank (RFB) [96] is to compute the CAF, Eq. (3) in a limited delay and Doppler interval of interest, avoiding any unnecessary processing. The RFB is made up by M correlation filters with their impulse responses related to the reference signal $g(t)$ as shown in Fig. 20. In reception, the surveillance signal $s(t)$ is divided into P contiguous sections of duration T_r: $s(t) = s_0(t) + s_1(t) + \ldots + s_{P-1}(t)$.

The first section $s_0(t)$ is sent as input to the RFB. The filter's outputs are coherently added creating a first single range profile. This process is repeated for the second section $s_1(t)$; being the reference signal delayed by T_r, a second range profile is generated. At the pth step, it results:

$$\tilde{R}_{\mathrm{sg}}^{(p)}(t) = s_p(t) \otimes \left[g_p(t) + g_{p+1}(t) + \ldots + g_{p+M-1}(t) \right] \tag{8}$$

Each $\tilde{R}_{\mathrm{sg}}^{(p)}(t)$, $p = 0, 1, \ldots, P - M$, represents a correlation function whose amplitude envelope is an isosceles trapezoid with major base $(M + 1)T_r$, minor base $(M - 1)T_r$ and height T_r. For $p = 1, \ldots, P - M$, each trapezoid is delayed by T_r with respect to the previous one. In order to cope with the maximum range requirement equal to $\mathrm{cMT}_r/2$, each $\tilde{R}_{\mathrm{sg}}^{(p)}(t)$, for $1 < p \leq P - M$, is realigned in time by compensating for the delay pT_r, and the coherent sum becomes:

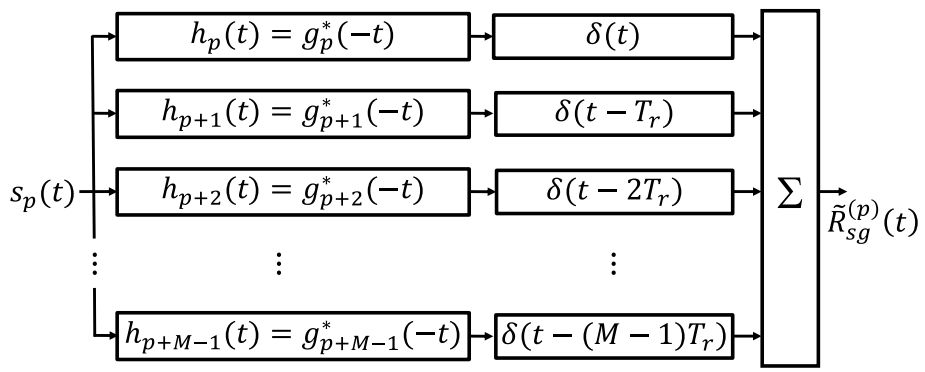

Fig. 20 Range filter bank (RFB). $\delta(t)$ denotes the delay

$$R_{\mathrm{sg}}(t) = \sum_{p=0}^{P-M} \tilde{R}_{\mathrm{sg}}^{(p)}(t + pT_r) \tag{9}$$

The envelope of the sum results in an isosceles trapezoid with major base $(M+1)T_r$, minor base $(M-1)T_r$ and height $(P-M+1)T_r$. The loss, in dB, with respect to the peak of the triangle (PT_r) is $L_{\mathrm{RFB}} = 10 \cdot \log_{10}\left(1 - \frac{M-1}{P}\right)[dB]$. To guarantee $L_{\mathrm{RFB}} < 1$ dB, P and M has to be: $M \leq \frac{P}{5} + 1$. Normally, due to the practical value of the maximum range of interest, $M \ll P$ and the L_{RFB} is negligible. The maximum range of the RFB is determined by the minor base of the trapezoid: $R_{\max} = (M-1)\frac{\mathrm{cT}_r}{2}$, while the correlation envelope reaches zero at $R_{\mathrm{tot}} = M\frac{\mathrm{cT}_r}{2}$, as shown in Fig. 21 for $P = 10$ and $M = 3$, where the abscissa reports the range normalized to $R_0 = \mathrm{cT}_r/2$. Note that a *fading* effect in the Mth range filter occurs with constant length of $R_{\mathrm{fade}} = R_{\mathrm{tot}} - R_{\max} = R_0$.

Each term of the sum in Eq. (9) represents a fast time processing with the aim of extracting range data. A data reorganization follows the processed data (realigning in time of the range profiles). An ensuing slow time processing has the aim to provide a further processing gain and to extract the Doppler radial velocity. In such a way, the only remaining losses are those due to the "Doppler mismatch" (constant phase in place of linear phase) within each interval of duration T_r, readable on the y-axis of Fig. 19, and made negligible with a suited choice of T_r. In [96], the parameter P is factorized in the product of the two integers N_Σ and $N_\mathcal{F}$, i.e., $P = N_\Sigma \cdot N_\mathcal{F}$. The first term N_Σ represents the number of coherent sums of range profiles (prior of the FFT operation). When $N_\Sigma > 1$, the number of FFT points $(N_\mathcal{F})$ is reduced accordingly for each range cell.

Considering the MTD processing as described in the Introduction, the RFB shows a high similitude with the MTD. Both processing methods use fast time/slow time $(L \times N)$ data matrix to extract range and Doppler parameters. With the same *CPI* and sampling interval of $1/B$ (with B the bandwidth of the signal), in RFB, $N = \frac{P}{M}$ and $L = M \cdot T_r \cdot B$.

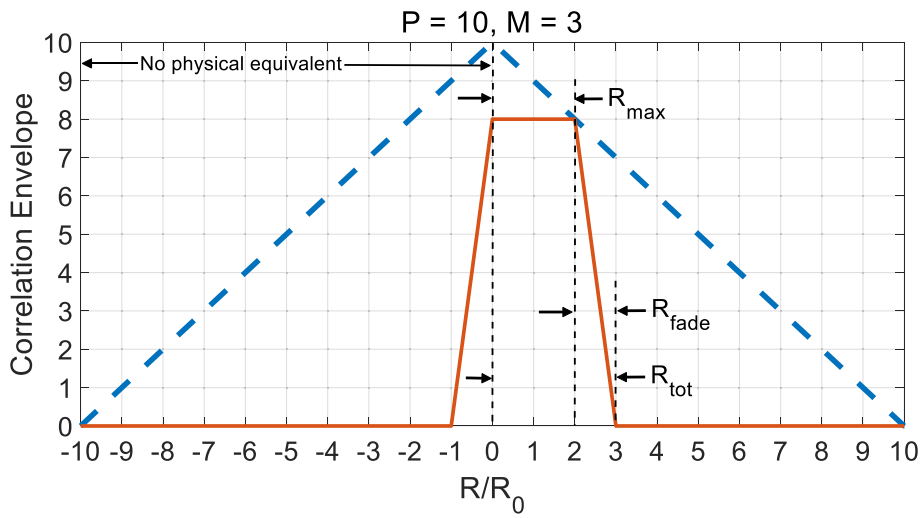

Fig. 21 Correlation envelope versus the normalized range: $P = 10, M = 3, R_0 = cT_r/2, L_{\mathrm{RFB}} = -0.97$ dB

7 Experimental results

7.1 Noise radar demonstrator

A noise radar demonstrator was developed at FHR during the past few years, which operates in the same frequency region of the X-band as standard marine navigation radars, i.e., between 9300 and 9400 MHz. This choice was made in order to enable experiments that include the coexistence of noise radars and the various emissions of commercial radars. The noise radar demonstrator follows the design criteria as described in Sect. 4 and, in principle, is capable of exploiting both the aforementioned choices for the reference signal. However, one has to notice that in most FHR experiments an analog reference signal taken at the X-band is preferred and that [3] makes use of the system's capability to compare both choices of reference signal on the same set of surveillance data.

An FPGA, a mass storage device and appropriate A/D and D/A converters form the digital core element of this demonstrator. A picture of this ensemble is displayed on the left-hand side of Fig. 22. The full demonstrator system (excluding the antennas) is shown on the right-hand side of the same figure. The upper tray of the displayed flight case contains the digital processor. The front end, whose principles and ports are described in Sect. 4, is located in the middle tray with ports W, S, R connected to the digital back end and ports Rx, Tx connected to the antennas by green, low-loss cables. The lower tray holds the local oscillator signal that is used by the mixers in the RF front end.

7.2 Some trials

To describe a part of the FHR trials, an experiment is presented that makes use of the efficient computation capabilities of the range filter bank (RFB, Sect. 6.3) and his moving target detection capabilities.

In the setup, the demonstrator was assembled into a car with antennas oriented in the direction opposite to the normal motion of the platform. This arrangement provides an optimal exploitation of the Doppler effect while preserving a safe control of the car by the driver. A second person inside the car is required as a radar operator. This setup of a noise radar and a significantly moving platform, as a novelty, was first described in [97]. The measurement system is displayed in Fig. 23 showing, on the left-hand side, the installation of the digital and RF components to the trunk of the

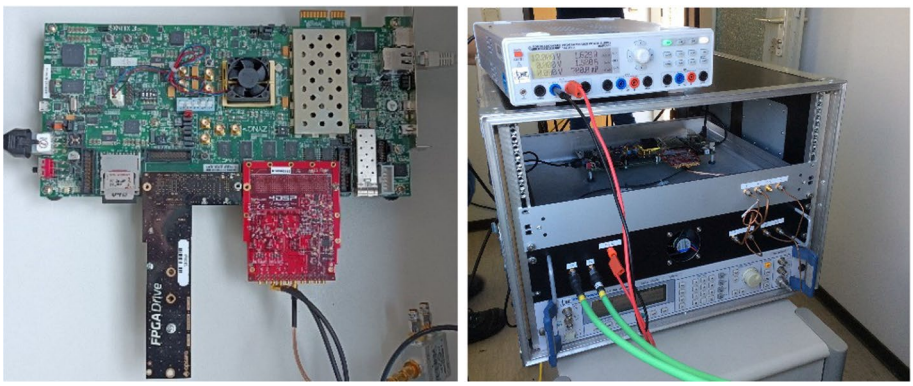

Fig. 22 Core elements of the digital back end (left) embodied in the upper tray of the demonstrator (right)

radar car. Next to these, a mobile power supply is contained. The right-hand side of Fig. 23 displays an outside view to the demonstrator arrangement with two standard horn antennas being mounted on each side of a microwave-isolating material block to the rear of the radar car.

The following measurements were performed when driving along a straight highway, an optimal setup for Doppler investigations as all motions are along a radial direction to the radar. Hence, a direct mapping of the tachometer values with the indicated Doppler shift gives a simple indicator for the verification of the moving target detection by the RFB. The set of experimental data was recorded in a hilly area at a point where the radar car was driven on one uphill side of a slight valley, whereas some targets were located on the opposite uphill side. This configuration minimized the mutual shadowing effect that may affect the signals from targets of similar size and shape when recorded along their arrangement in a row.

The experimental environment includes static targets (trees and the guardrails of the highway). In the same direction in which the radar car drove, there were slower road users, but due to the higher traffic volume, no car was expected to drive faster than the radar car. On the other lane, driving in the opposite direction, the situation also consists of two groups of road users, a slower and a faster one. However, all cars of each group drove with approximately the same speed. Figure 24 shows a picture of a similar road situation photographed by the radar operator.

This arrangement of targets can be detected and displayed from the radar results as shown in Fig. 25. The range–Doppler map shows the distance to the targets on its x-axis and the Doppler frequency, converted to radial velocity of the targets on its y-axis. Here, the Doppler values face an offset due to the proper motion of the radar platform. When taking into account that the velocity of the radar platform was equal to $v_p = 130$ km/h, all static targets are expected to show an indicated velocity of -130 km/h and, indeed, the j-hook-shaped clutter returns converge against this value for grater ranges. Consequently, all targets at speeds similar to v_p appear at relative velocity values close to zero, a region in the range–Doppler map that is highly affected by leakage effects between the transmitter and the receiver as explained in Sect. 4 and in [98]. Note that cars moving on the opposite lane produce distinct target echoes in the range–Doppler map that are neither affected by leakage nor by clutter effects.

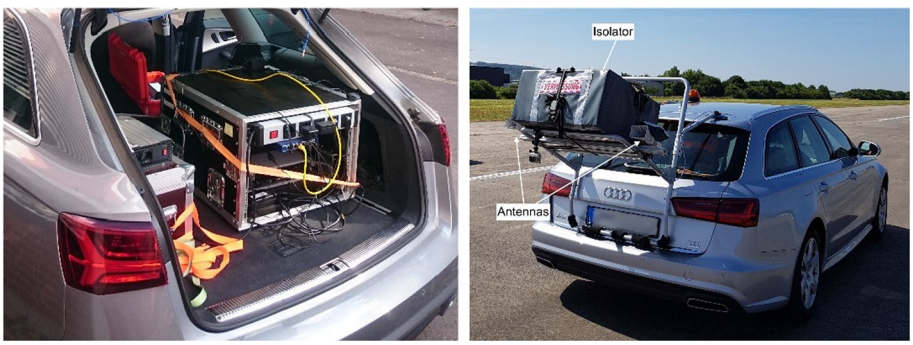

Fig. 23 Assembly of the demonstrator to a moving platform. The antennas are mounted to the rear of the car, whereas the main parts of the demonstrator are fixed inside the trunk of the car along with a mobile power supply

Fig. 24 A road situation similar to the one that was recorded by the radar

In Fig. 25, the slower group of road users is indicated by a dashed rectangular frame. Their relative velocity is measured to be −212 km/h and when compensating for the platform speed v_p, the actual velocity of this group is in the order of 80 km/h which is a typical speed of trucks in high traffic situations on German highways. Three other cars were measured at different speed levels. Their echoes are highlighted by solid circular frames in Fig. 25. The results indicate an overtaking process at the distance of 275 m where there are two reflections at different Doppler shifts. One belongs to the group of slower road user at 80 km/h, and the other one, at a higher Doppler level, corresponds to an overtaking car with an actual velocity of 120 km/h.

These experiments evidentiate the high suitability of noise radar technology for moving target detection. In the past, the beneficial absence of range and Doppler ambiguities in noise radar was contradicted by the high computation load that the CAF requires. The

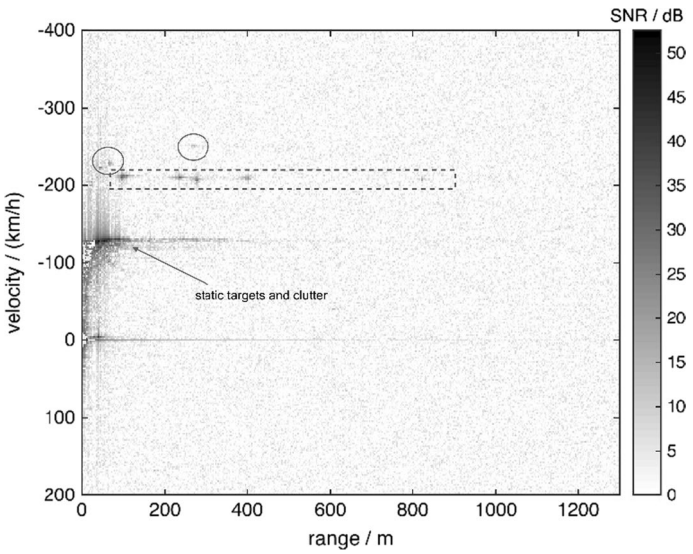

Fig. 25 Resulting range–Doppler map. All velocities are drawn relative to the proper motion of the radar platform. Due to the antenna arrangement, the static clutter appears at negative relative velocities. Two groups of road users are highlighted by either a dashed box or solid circles

latter may be replaced by the much more efficient range filter bank (RFB) algorithm enabling the use of the NRT in resource-limited applications.

Please note that the SNR of the targets in this measurement was increased by reducing damaging effects of strong close-in clutter returns and direct leakage using the ECA-T [99] algorithm producing "white spots" in the range–Doppler cells, to which the ECA-T is applied.

8 Conclusions

This tutorial on noise radar technology has presented, in addition to the main historical elements and to the basic operating principles, some selected and recent scientific advancements in both the theoretical and the experimental arenas. The presentation might encourage further research in this stimulating area as well as the operational use of (pseudo) random signals in future radar systems. Having known and understood the specific capabilities of noise radar for many decades, science carries on to remove the practical hurdles and some preconceptions (biases) that still today impede the industrialization of noise radar technology in many practical applications. For example, one exemplary preconception is the sometime alleged *"ten dB loss"* due to the random modulation of the transmitted signal; however, it was shown to be possible to make this loss smaller and smaller by imposing a suitable PAPR to the *"tailored"* waveform.

The authors believe that the results presented in this paper will serve as enablers along this aspiring way.

Abbreviations

ACF	Auto-correlation function
ADC	Analog-to-digital converter
AF	Ambiguity function
AI	Artificial intelligence
AWG	Arbitrary waveform generator
CAF	Cross-ambiguity function
CCF	Cross-correlation function
CNN	Convolutional neural network
COSPAR	Combined spectral shaping and peak-to-average power ratio reduction
CPI	Coherent processing interval
CRSS	Communication and radar spectrum sharing
DAC	Digital-to-analog converter
DFT	Discrete Fourier transform
ELINT	Electronic intelligence
ES	Electronic support
EW	Electronic warfare
FFT	Fast Fourier transform
FM-CW	Frequency modulation continuous waveform
FPGA	Field-programmable gate array
HNLFM	Hybrid nonlinear frequency modulation
IF	Intermediate frequency
IFFT	Inverse fast Fourier transform
IID	Independent identically distributed
LFM	Linear frequency modulation
LPE	Low probability of exploitation
LPI	Low probability of intercept
MIMO	Multiple-input, multiple-output
MTD	Moving target detector
NATO	North Atlantic Treaty Organization
NLFM	Nonlinear frequency modulation
NRT	Noise radar technology
PAPR	Peak-to-average power ratio
PRI	Pulse repetition interval
PRN	Pseudo-random number
PRNGs	Pseudo-random number generators

PRT	Pulse repetition time
PSL	Peak sidelobe level
RF	Radio frequency
RFB	Range filter bank
RSR	Random signals radar
RTG	Research task groups
RWR	Radar warning receivers
SAR	Synthetic aperture radar
SEI	Specific emitter identification
SNR	Signal-to-noise ratio
STO	Science and Technology Organization
TNRCC	Turkish Naval Research Center Command
WRT	Waveform recognition technique

Acknowledgements
The authors are grateful to the NATO Research Task Groups SET-225 and SET-287 for being the "umbrella" of this research. We also wish to thank the referees for their constructive comments.

Author contributions
GG and GP mostly contributed to the description of radar waveforms (both deterministic and random), the historical overview of noise radar technology and the generation of noise waveforms. CW mostly contributed to the laboratory and field trials and to the novel processing algorithm (range filter bank). All authors contributed to the description and presentation of the results. All authors read and approved the final manuscript.

Funding
No funding from external bodies: basic expenses have been paid by the employers.

Availability of data and materials
Not applicable/no data available for sharing.

Declarations

Ethics approval and consent to participate
Not applicable.

Consent for publication
Not applicable.

Competing interests
The authors do not have any competing interest.

Received: 7 March 2022 Accepted: 1 June 2022
Published online: 21 June 2022

References

1. G Galati, G Pavan, C Wasserzier, K Savci, Introduction to Noise Radar and its Waveforms, MDPI Special Issue on Noise Radar Technology: System Design, Demonstrations and Characterization (NRT-SDC), MDPI Sensors 2020, 20(18), 5187 (2020). https://doi.org/10.3390/s20185187.
2. K. Savci, A.G. Stove, F. De Palo, A.Y. Erdogan, G. Galati, K.A. Lukin, S. Lukin, P. Marques, G. Pavan, C. Wasserzier, Noise radar-overview and recent developments. IEEE Aerosp. Electron. Syst. Mag. (2020). https://doi.org/10.1109/MAES.2020.2990591
3. G Galati, G Pavan, K Savci, C Wasserzier, Noise Radar Technology: waveforms Design and Field Trials, MDPI Special Issue on Noise Radar Technology: System Design, Demonstrations and Characterization (NRT-SDC), Sensors (2021), 21(9), 3216. https://doi.org/10.3390/s21093216.
4. M.A. Richards, *Fundamentals of Radar Signal Processing* (McGraw-Hill Electronic Engineering, New York, 2005)
5. C.E. Muehe, The moving target detector. IEEE Trans. Aerosp. Electron. Syst. (2006). https://doi.org/10.1109/TAES.2006.248219
6. D Qiaona, T Yonghua, Optimal Design of MTD Filter Based on FIR, in Proceedings of International Conference on Signal, Information and Data Processing (ICSIDP), (2019), https://doi.org/10.1109/ICSIDP47821.2019.9173469.
7. E. D'Addio, G. Galati, Adaptivity and design criteria of a latest-generation MTD processor. IEE Proc. F Commun. Radar Signal Process. **132**, 58–65 (1985). https://doi.org/10.1049/ip-f-1.1985.0007
8. J.R. Klauder, A.C. Price, S. Darlington, W.J. Albefsheim, The theory and design of chirp radars. Bell Syst. Tech. J. **39**(4), 745–808 (1960)
9. N. Levanon, E. Mozeson, *Radar Signals* (John Wiley & Sons Inc., Hoboken, 2004)
10. A.H. Nuttall, Some windows with very good sidelobe behaviour. IEEE Trans. Acoust. Speech Signal Process **29**, 84–91 (1981)
11. AW Doerry, Generating Nonlinear FM Chirp Waveforms for Radar", Sandia Report SAND2006-5856, (2006).

12. R.E. Millett, A matched filter pulse-compression system using a nonlinear FM waveform. IEEE Trans. Aerosp. Electron. Syst. **AES-6**, 73–77 (1970)
13. T. Collins, P. Atkins, Nonlinear frequency modulation chirp for active sonar. IEE Proc. Radar Sonar Navig. **146**, 312–316 (1999)
14. Z Ge, P Huang, W Lu, Matched NLFM Pulse Compression Method with Ultra-low Sidelobes, in Proceedings of the 5th European Radar Conference, Amsterdam, October (2008), pp. 92–95.
15. G Galati, G Pavan, Optimal chirp waveforms for long/medium range surveillance radar, in Proceedings of the16th International Radar Symposium (2015), Germany. https://doi.org/10.1109/IRS.2015.7226308.
16. P.M. Woodward, *Probability and Information Theory with Applications To Radar* (Mc Graw Hill, New York, 1953)
17. D Eustice, C. Baylis, J Marks, Woodward's ambiguity function: From foundations to applications, Texas Symposium on Wireless and Microwave Circuits and Systems (2015), pp. 1–17. https://doi.org/10.1109/WMCaS.2015.7233208.
18. N. Zhang, S.W. Golomb, Polyphase sequence with low autocorrelations. IEEE Trans. Inf. Theory **39**, 1085–1089 (1993)
19. R.H. Barker, *Group Synchronization of Binary Digital Systems* (Academic Press, London, 1953)
20. R.L. Frank, S.A. Zadoff, Phase shift pulse codes with good periodic correlation properties. IRE Trans. Inf. Theory **IT-8**, 381–382 (1962)
21. J.P. Costas, A study of a class of detection waveforms having nearly ideal range-Doppler ambiguity properties. Proc. IEEE **72**, 996–1009 (1984)
22. K Iwasa, T Kishigami, H Yomo, A Matsuoka, J Satou, MIMO radar system using orthogonal complementary codes with Doppler offset, in Proceedings of the European Radar Conference, (2017), Nuremberg, Germany, pp. 102–105. https://doi.org/10.23919/EURAD.2017.8249157.
23. G. Galati, G. Pavan, Range sidelobes suppression in pulse-compression radar using Golay pairs: some basic limitations for complex targets. IEEE Trans. Aerosp. Electron. Syst. **48**(3), 2756–2760 (2012). https://doi.org/10.1109/TAES.2012.6237627
24. G. Galati, G. Pavan, Waveforms design for modern and MIMO radar. Proc. Eurocon (2013). https://doi.org/10.1109/EUROCON.2013
25. G. Galati, *100 years of radar* (Springer, Cham, 2016)
26. M. Modarres-Hashemi, M.M. Nayebi, LPD feature improvement in random PRF radar signals. IEE Proc. Radar Sonar Navig. **151**(4), 225–230 (2004)
27. X. Long, K. Li, J. Tian, J. Wang, S. Wu, Ambiguity function analysis of random frequency and PRI agile signals. IEEE Trans. Aerosp. Electron. Syst. **57**(1), 382–396 (2021)
28. C.E. Cook, M. Bernfeld, *Radar Signals: An Introduction to Theory and Applications* (Artech House, Norwood, 1993)
29. KA Lukin, Millimeter wave noise radar applications: theory and experiments, in Proceedings of MSMW'2001, Kharkov, Ukraine, (2021), pp. 68–73.
30. M. Matsumoto, T. Nishimura, Mersenne Twister: a 623-dimensionally equidistributed uniform pseudo-random number generator. ACM Trans. Model. Comput. Simul. **8**, 3–30 (1998)
31. G. Galati, G. Pavan, K. Savci, C. Wasserzier, Counter-interception and counter-exploitation features of noise radar technology. Remote Sens. (2021). https://doi.org/10.3390/rs13224509
32. P.E. Pace, *Detecting and Classifying Low Probability of Intercept Radar*, 2nd edn. (Edn Artech House Remote Sensing Library, Norwood, 2008)
33. Y.C. Lang, *Dynamic Spectrum Management-From Cognitive Radio to Blockchain and Artificial Intelligence* (Springer, Berlin, 2020). https://doi.org/10.1007/978-981-15-0776-2
34. P. Stoica, J. Li, X. Zheng, Signal synthesis and receiver design for MIMO radar imaging. IEEE Trans. Signal Process. **56**, 3959–3967 (2008)
35. G. Galati, G. Pavan, F. De Palo, Compatibility problems related with pulse-compression, solid-state marine radars. IET Radar Sonar Navig. **10**, 791–797 (2016). https://doi.org/10.1049/iet-rsn.2015.0400
36. A. De Martino, *Introduction to Modern EW Systems*, 2nd edn. (Artech House, Norwood, 2018)
37. D. Adamy, *EW101–A first Course in Electronic Warfare* (Artech House, Norwood, 2001)
38. D. Adamy, *EW102–A Second Course on Electronic Warfare* (Artech House, Norwood, 2004)
39. D. Adamy, *EW103–Tactical Battlefield Communication Electronic Warfare* (Artech House, Norwood, 2008)
40. D. Adamy, *EW104–EW Against New Generation of Threats* (Artech House, Norwood, 2015)
41. R.A. Poisel, *Electronic Warfare Target Localization Methods* (Artech House, Norwood, 2012)
42. D. Curtis Schleher, *Electronic Warfare in the Information Age* (Artech House, Norwood, 1999)
43. R.G. Wiley, *ELINT-The Interception and Analysis of Radar Signals* (Artech House, Norwood, 2006)
44. J. Bao-Yen Tsui, *Microwave Receivers with Electronic Warfare Applications* (Krieger Publishing Company, Malabar, 1992)
45. P Tucker, Cognitive EW: This Is The Most Important Technology On the F-35", Defense One, Jannuary (2016).
46. W.W. Goj, *Synthetic Aperture Radar and Electronic Warfare* (Artech House, Norwood, 1993)
47. TC Oroian, F Enache, P Ciotirnae, Some considerations about third-order statistics for different types of radar signals, in Proceedings of the 10th Intern. Symposium on Advanced Topics in Electrical Engineering, (2017), Bucharest, Romania. https://doi.org/10.1109/ATEE.2017.7905090
48. A.O. Alyt, A. Omar, A. Elsherbeni, Detection and localization of RF radar pulses in noise environments using wavelet packet transform and higher order statistics. Prog. Electromagn. Res. **58**, 301–317 (2006). https://doi.org/10.2528/PIER05070204
49. S Barbarossa, Parameter estimation of undersampled signals by Wigner–Ville analysis, in Proceedings of IEEE Conference Acoust. Speech Signal Process, ICASSP 91 (2002), 5, 3944–3947.
50. TO Gulum, PE Pace, R Cristi, Extraction of Polyphase Radar Modulation Parameters Using a Wigner-Ville Distribution Radon Transform, in Proceedings of the IEEE International Conference on Acoustics, Speech and Signal Processing, (2008). https://doi.org/10.1109/ICASSP.2008.4517907.

51. DB Copeland, PE Pace, Detection and analysis of FMCW and P-4 polyphase LPI waveforms using quadrature mirror filter trees, in Proceedings of the IEEE International Conference on Acoustics, Speech, and Signal Processing, (2002) IV-3960–IV-3963. https://doi.org/10.1109/ICASSP.2002.
52. R.S. Roberts, W.A. Brown, H.H. Loomis, Computationally efficient algorithms for cyclic spectral analysis. IEEE Signal Process. Mag. **8**, 38–49 (1991). https://doi.org/10.1109/79.81008
53. H.F. Kookamari, Y. Norouzi, M.M. Nayebi, Using a moving aerial platform to detect and localise a low probability of intercept radar. IET Radar Sonar Navig. **11**, 1062–1069 (2017). https://doi.org/10.1049/iet-rsn.2016.0295
54. H.F. Kookamari, Y. Norouzi, E.S. Kashani, M.M. Nayebi, A novel method to detect and localize LPI radars. IEEE Trans. Aerosp. Electron. Syst. **55**, 2327–2336 (2019). https://doi.org/10.1109/TAES.2018.2885109
55. S.H. Kong, M.M. Kim, L.M. Hoang, E. Kim, Automatic LPI radar waveform recognition using CNN. IEEE Access **6**, 4207–4219 (2018). https://doi.org/10.1109/ACCESS.2017.2788942
56. A Aubry, A Bazzoni, V Carotenuto, A De Maio, P Failla, Cumulants-based Radar Specific Emitter Identification, in Proceedings of IEEE International Workshop on Information Forensics and Security, (2011), Iguacu Falls (Brazil). https://doi.org/10.1109/WIFS.2011.6123155.
57. R Ardoino, A Megna, LPI Radar detection: SNR performances for a dual channel Cross-Correlation based ESM Receiver, in Proceedings of European Radar Conference–EuRAD (2009), Rome.
58. J.A. Tropp, I.S. Dhillon, R.W. Heath, T. Strohmer, Designing structured tight frames via an alternating projection method. IEEE Trans. Inf. Theory **51**(1), 188–209 (2005)
59. F De Palo, Noise radar technology: Waveforms, Architecture, Applications, PhD dissertation, Tor Vergata University of Rome XXIX Cycle (2017). ISBN: 978-88-903482-5-9.
60. T.M. Cover, J.A. Thomas, *Elements of Information Theory*, 2nd edn. (John Wiley and Sons, Inc., Hoboken, 2006)
61. B.M. Horton, Noise-modulated distance measuring systems. Proc. IRE **49**, 821–828 (1959)
62. KA Lukin, RM Narayanan, Historical overview and current research on noise radar, in Proceedings of the 3rd International Asia-Pacific Conference on Synthetic Aperture Radar-APSAR, (2011).
63. KA Lukin, Millimiter Noise Radar Technology, in Proceedings of MSMW'98, Kharkov, Ukraine, (1998), pp. 94–97.
64. L. Guosui, H. Gu, The present and the future of random signal radars. IEEE Aerosp. Electron. Syst. Mag. **12**(10), 35–40 (1997). https://doi.org/10.1109/62.624326
65. L. Guosui, G. Hong, S. Weimin, Development of random signal radars. IEEE Trans. Aerosp. Electron. Syst. **35**(3), 770–777 (1999). https://doi.org/10.1109/7.784050
66. R.M. Narayanan, Y. Xu, P.D. Hoffmeyer, J.O. Curtis, Design, performance, and implementation of a coherent ultrawideband random noise radar. Opt. Eng. **37**(6), 1855–1869 (1998). https://doi.org/10.1117/1.601699
67. R.M. Narayanan, M. Dawood, Doppler estimation using a coherent ultra wide-band random noise radar. IEEE Trans. Antennas Propagation **48**, 868–878 (2000)
68. X. Xu, R.M. Narayanan, Range sidelobe suppression technique for coherent ultra-wideband random noise radar imaging. IEEE Transactions Antennas Propag. **49**, 1836–1842 (2001)
69. KA Lukin, Developments of Noise Radar Technology in LNDES IRE NASU, in Proceedings od the First International Workshop on the Noise Radar Technology, NTRW (2002), pp. 90–96.
70. KA Lukin, The Principles of Noise Radar Technology, First International Workshop on the Noise Radar Technology, NTRW (2002), pp. 13–22.
71. AW Doerry, B. Marquette, Random-phase radar waveforms with shaped spectrum, Sandia Report SAND2013-1450C, SPIE (2013) Defense, Security & Sensing Symposium, 8714.
72. S.R.J. Axelsson, Noise radar using random phase and frequency modulation. IEEE Trans. Geosci. Remote Sens. **42**(11), 2370–2384 (2004)
73. L. Pralon, B. Pompeo, J.M. Fortes, Stochastic analysis of random frequency modulated waveforms for noise radar systems. IEEE Trans. Aerosp. Electron. Syst. **51**(2), 1447–1461 (2015)
74. G. Galati, G. Pavan, On Phase folding in random phase/frequency modulation for noise radar. IEEE Geosci. Remote Sens. Lett. (2019). https://doi.org/10.1109/LGRS.2018.2886065
75. M. Malanowski, K. Kulpa, Detection of moving targets with continuous-wave noise radar: theory and measurements. IEEE Trans. Geosci. Remote Sens. **50**(9), 3502–3509 (2012). https://doi.org/10.1109/TGRS.2011.2181521
76. J.S. Kulpa, Ł Maślikowski, M. Malanowski, Filter-Based Design of Noise Radar Waveform With Reduced Sidelobes. IEEE Trans. Aerosp. Electron. Syst. **53**(2), 816–825 (2017). https://doi.org/10.1109/TAES.2017.2665145
77. AG Stove, G Galati, G Pavan, F De Palo, KA Lukin, K Kulpa, JS Kulpa, Ł Maślikowski, The NATO SET-184 noise radar trials 2016, in Proceedings of 17th International Radar Symposium, (2016), Krakow (Poland).
78. G Galati, G Pavan, F De Palo, AG Stove, Potential applications of noise radar technology and related waveform diversity, in Proceedings of 17th International Radar Symposium, (2016), Krakow (Poland).
79. AG Stove, G Galati, F De Palo, C Wasserzier, YA Erdogan, K Savci, KA Lukin, Design of a noise radar demonstrator, in Proceedings of 17th International Radar Symposium, (2016), Krakow (Poland).
80. C Wasserzier, AG Stove, KA Lukin, Verification of a continuous wave noise radar, in Proceedings of International Radar Symposium IRS (2019), Ulm, Germany.
81. K Savci, AG Stove, AY Erdogan, G Galati, KA Lukin, G Pavan, C Wasserzier, Trials of a Noise-Modulated Radar Demonstrator– First Results in a Marine Environment, in Proceedings of International Radar Symposium IRS (2019), Ulm, Germany.
82. K. Kulpa, *Signal Processing in Noise Waveform Radar* (Artech House, Norwood, 2013)
83. G. Galati (Editor), Radar evolution: the Italian academic contribution, CNIT Technical Report-02, (2019), ISBN 978-88-949-8217-6.
84. NIST Special Publication (SP) 800-90B. Recommendation for the Entropy Sources Used for Random Bit Generation, (2018), 100 Bureau Drive Gaithersburg, MD, USA. https://doi.org/10.6028/NIST.SP.800-90B.
85. S. Harase, On the F2-linear relations of Mersenne Twister pseudorandom number generators. Math. Comput. Simul. **100**, 103–113 (2014). https://doi.org/10.1016/j.matcom.2014.02.002
86. S Vigna, It is high time we let go of the Mersenne Twister, Comput. Sci. Data Struct. Algorithms (2019), Available online: https://arxiv.org/pdf/1910.06437. Accessed 10 Jan 2022.

87. M.A. Govoni, Range-Doppler resolution of the linear-FM noise radar waveform. IEEE Trans. Aerosp. Electron. Syst. **49**, 658–664 (2013)
88. M.A. Govoni, Low probability of intercept of an advanced noise radar waveform with linear-FM. IEEE Trans. Aerosp. Electron. Syst. **49**, 1351–1356 (2013)
89. G. Galati, G. Pavan, F. De Palo, Chirp signals and noisy waveforms for solid-state surveillance radars. MDPI Aerosp. **4**(1), 1–15 (2017). https://doi.org/10.3390/aerospace4010015
90. G. Galati, G. Pavan, Computer simulation of weather radar signals. Simul. Pract. Theory **3**, 17–44 (1995)
91. H. He, J. Li, P. Stoica, *Waveform Design for Active Sensing Systems–A Computational Approach* (Cambridge University Press, Cambridge, 2012)
92. G Galati, G Pavan, On the design of waveforms for noise-MIMO radar, in Proceedings of Noise Radar Technology (NRT), Yalta, Ukraine, (2012), pp.1–7.
93. JS Kulpa, Mismatched Filter for Range Sidelobes Suppression of Pseudo-Noise Signals, in Proceedings of Signal Processing Symposium–SPSympo, (2015), Debe (PL). https://doi.org/10.1109/SPS.2015.7168290.
94. K. Savci, G. Galati, G. Pavan, Low-PAPR waveforms with shaped spectrum for enhanced low probability of intercept noise radars. MDPI Remote Sens. **13**(12), 2372 (2021). https://doi.org/10.3390/rs13122372
95. G Galati, G Pavan, C Wasserzier, Optimal Processing in Noise Radar: Implementation Problems, in Proceedings of Signal Processing Symposium, (2019), Krakow (PL). https://doi.org/10.1109/SPS.2019.8882098.
96. C. Wasserzier, G. Galati, On the efficient computation of range and Doppler data in noise radar. Int. J. Microw. Wirel. Technol. **11**(7), 584–592 (2019). https://doi.org/10.1017/S175907871800171X
97. C. Wasserzier, G. Galati, First experimental results on the feasibility of noise radar systems on fast moving platforms. Electron. Lett. **55**(6), 344–345 (2019)
98. C Wasserzier, G Galati, Measuring the Isolation of a Continuous Emission Radar by Support of the Doppler Effect, in Proceedings of IEEE 7th International Workshop on Metrology for AeroSpace, (2020), 7–11. https://doi.org/10.1109/MetroAeroSpace48742.2020.9160180
99. C Wasserzier, P Wojaczek, D Cristallini, J Worms, D O'Hagan, Doppler-Spread Clutter Suppression in Single-Channel Noise Radar, in Proceedings of International Radar Conference, (2019), https://doi.org/10.1109/RADAR41533.2019.171219.

Publisher's Note